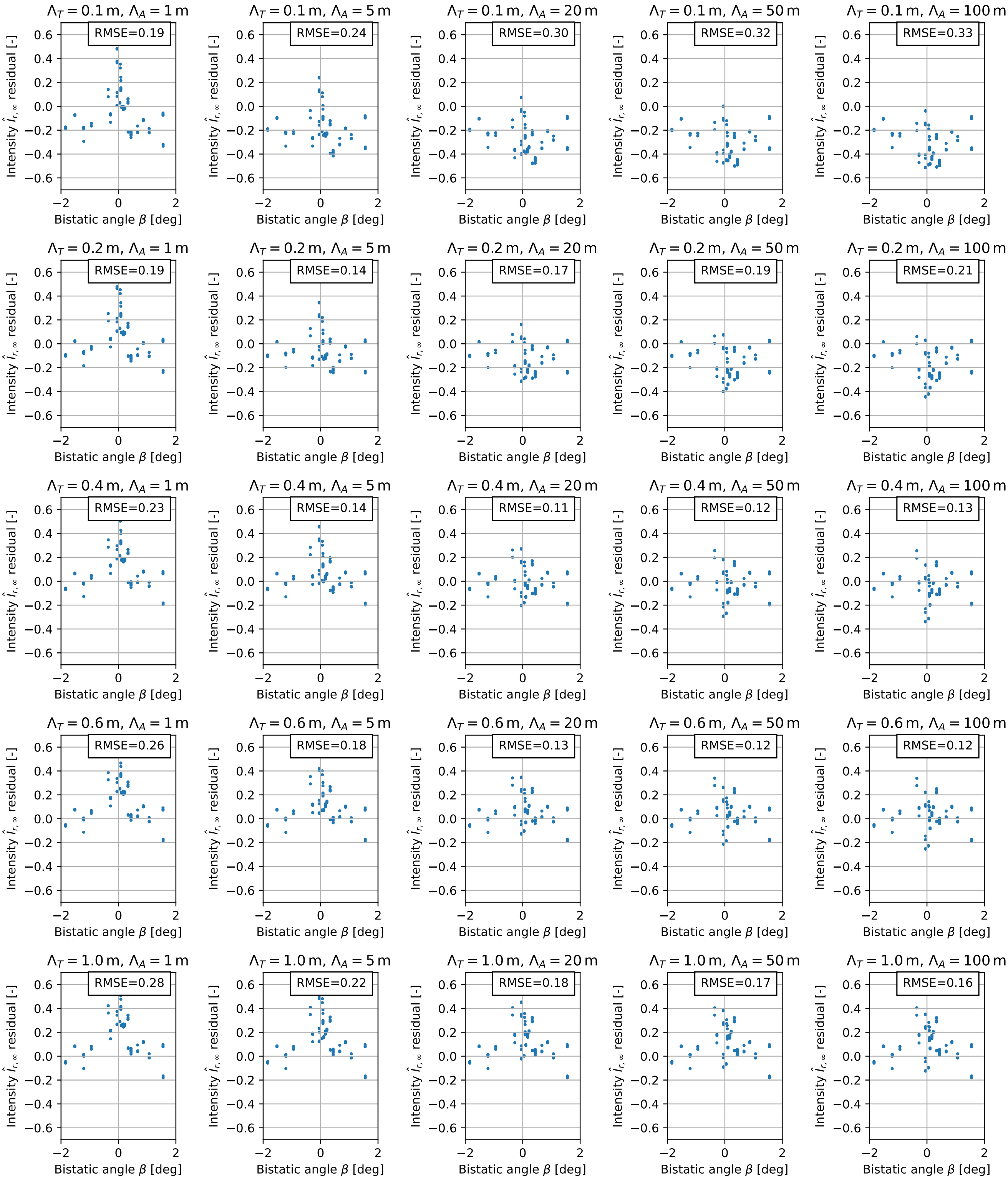

Figure S1. Plots of residuals of winter KAPRI measurements in the VV polarimetric channel, with varying values of model parameters Λ_T (constant along rows) and Λ_A (constant along columns). The residual was computed as the difference between observed value of $\hat{I}_{\mathrm{r},\infty}$ and value predicted by the model $I_{\mathrm{r},\infty}$ defined by parameters Λ_T, Λ_A, at the corresponding bistatic angle β.

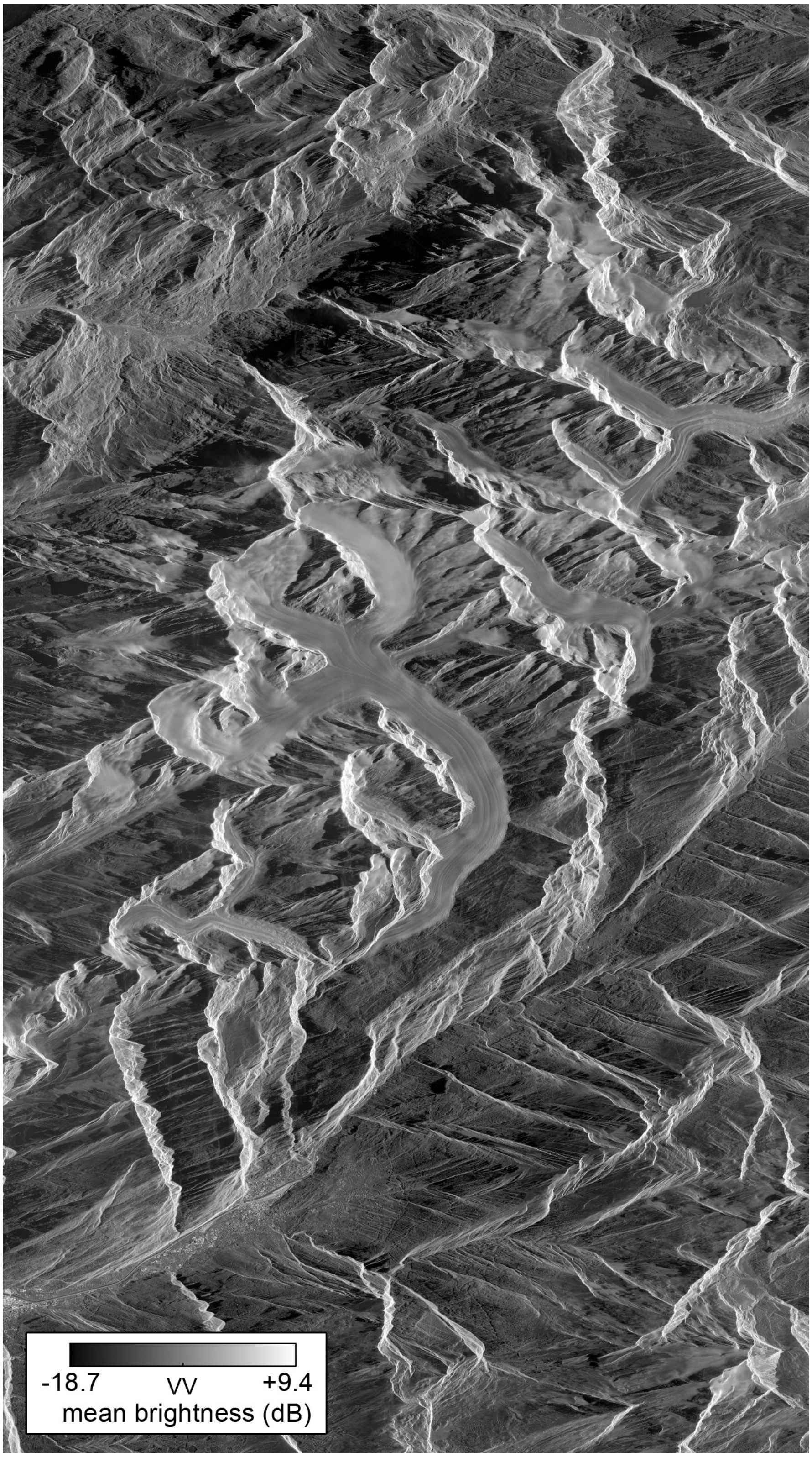

Figure S2. Intensity average of 118 TanDEM-X acquisitions of the Jungfrau-Aletsch region (VV polarization). The image has been flipped/rotated to align approximately with the north-direction. The slant-range direction is from right to left; azimuth from top to bottom.

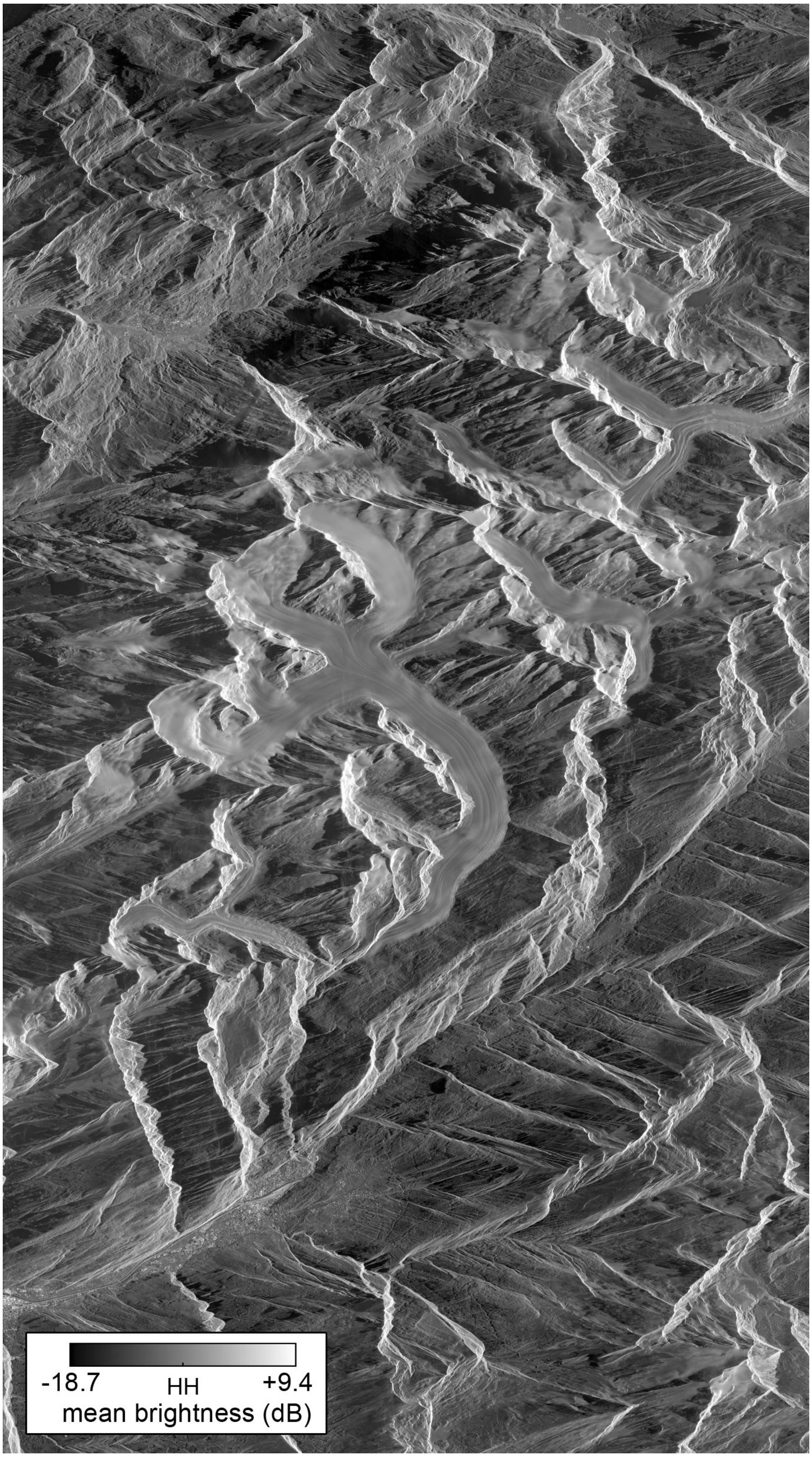

Figure S3. Intensity average of 118 TanDEM-X acquisitions of the Jungfrau-Aletsch region (HH polarization). The image has been flipped/rotated to align approximately with the north-direction. The slant-range direction is from right to left; azimuth from top to bottom.

Figure S4. The backscatter ratio $\hat{I}^{\mathrm{uncal.}}_{\mathrm{r,0,VV}}$ of the temporal mean of 17 acquisitions with a baseline $b < 300\,\mathrm{m}$ for the VV polarization. Narrow areas following mountain ridges show values deviating more than 5% from unity.

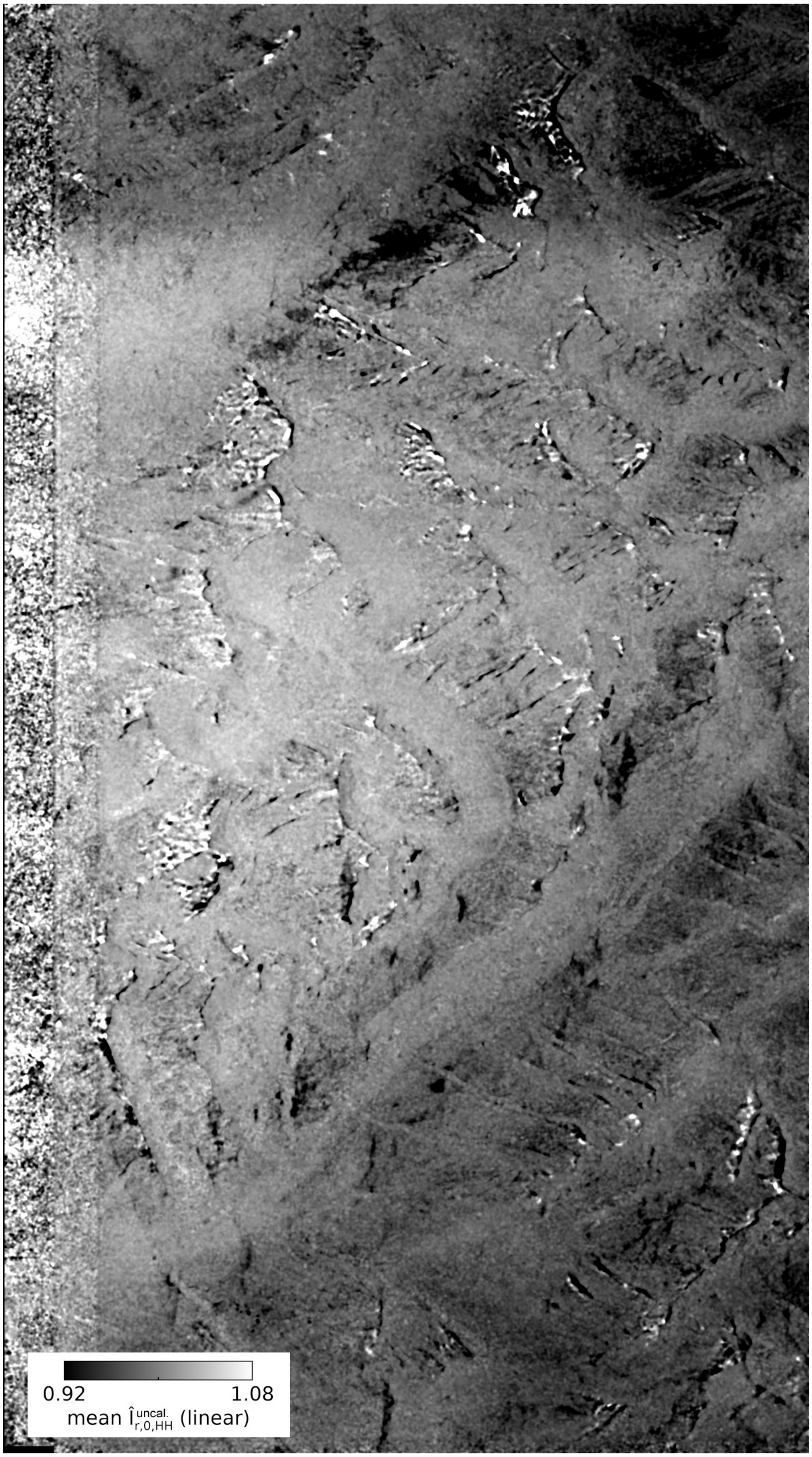

Figure S5. The backscatter ratio $\hat{I}^{\text{uncal.}}_{\text{r,0,HH}}$ of the temporal mean of 17 acquisitions with $b < 300\,\text{m}$ shows a strong spatial variability likely due to an uncompensated antenna pattern. Narrow areas following mountain ridges show values deviating more than 5% from unity.

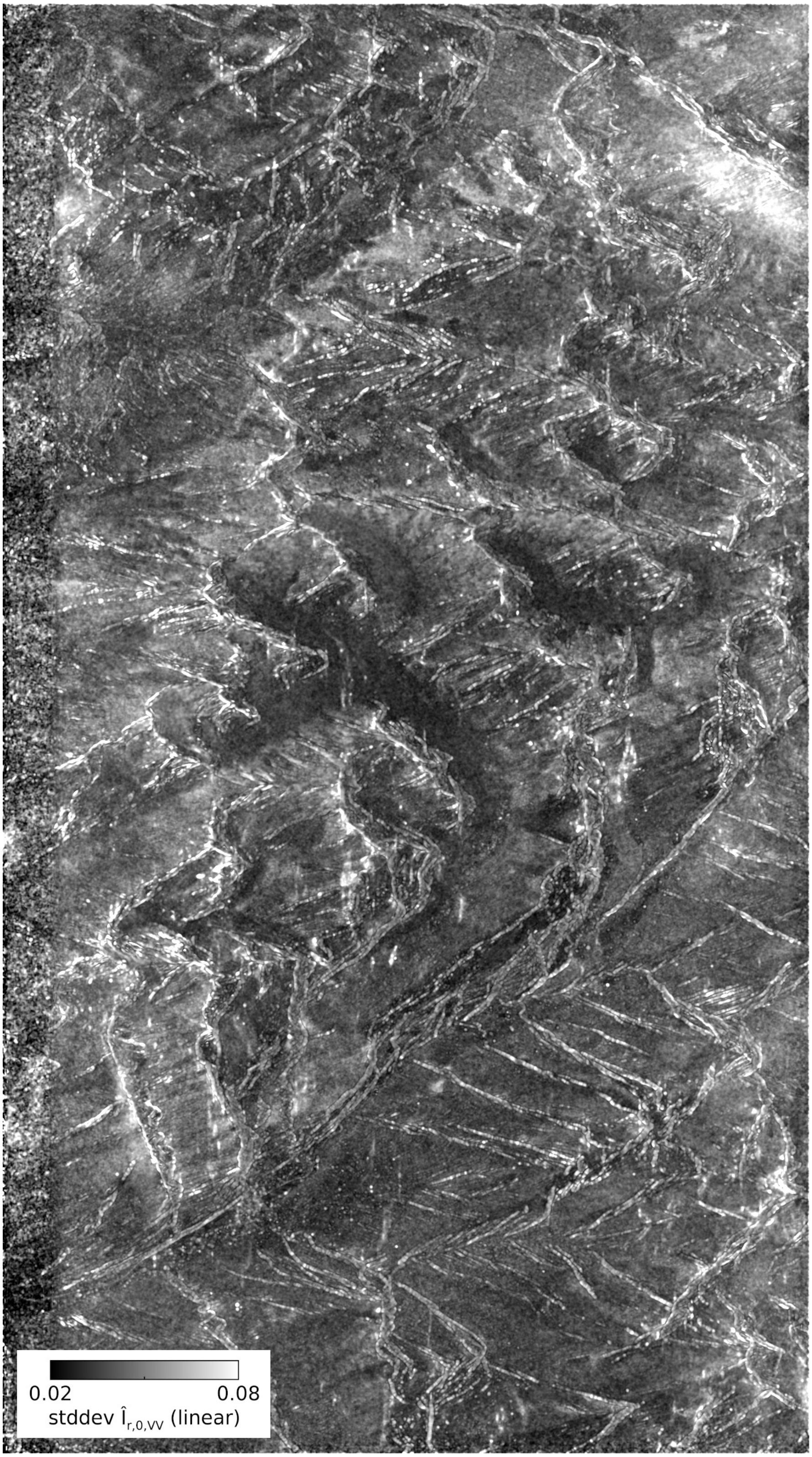

Figure S6. Temporal standard deviation of the backscatter ratio $\hat{I}_{r,0}$ (VV) of all 118 acquisitions after correction for atenna pattern.

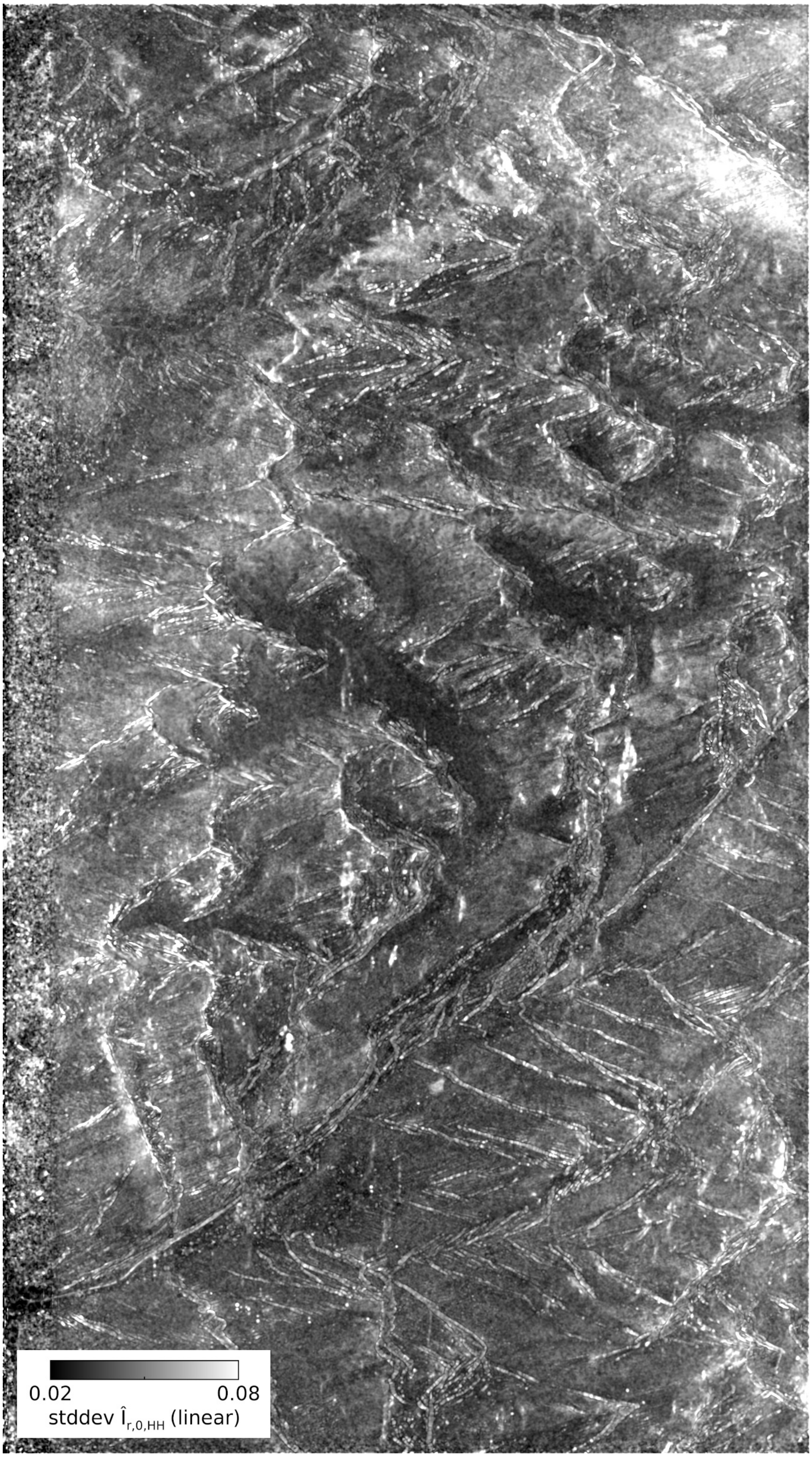

Figure S7. Temporal standard deviation of the backscatter ratio $\hat{I}_{r,0}$ (HH) of all 118 acquisitions after correction for atenna pattern.

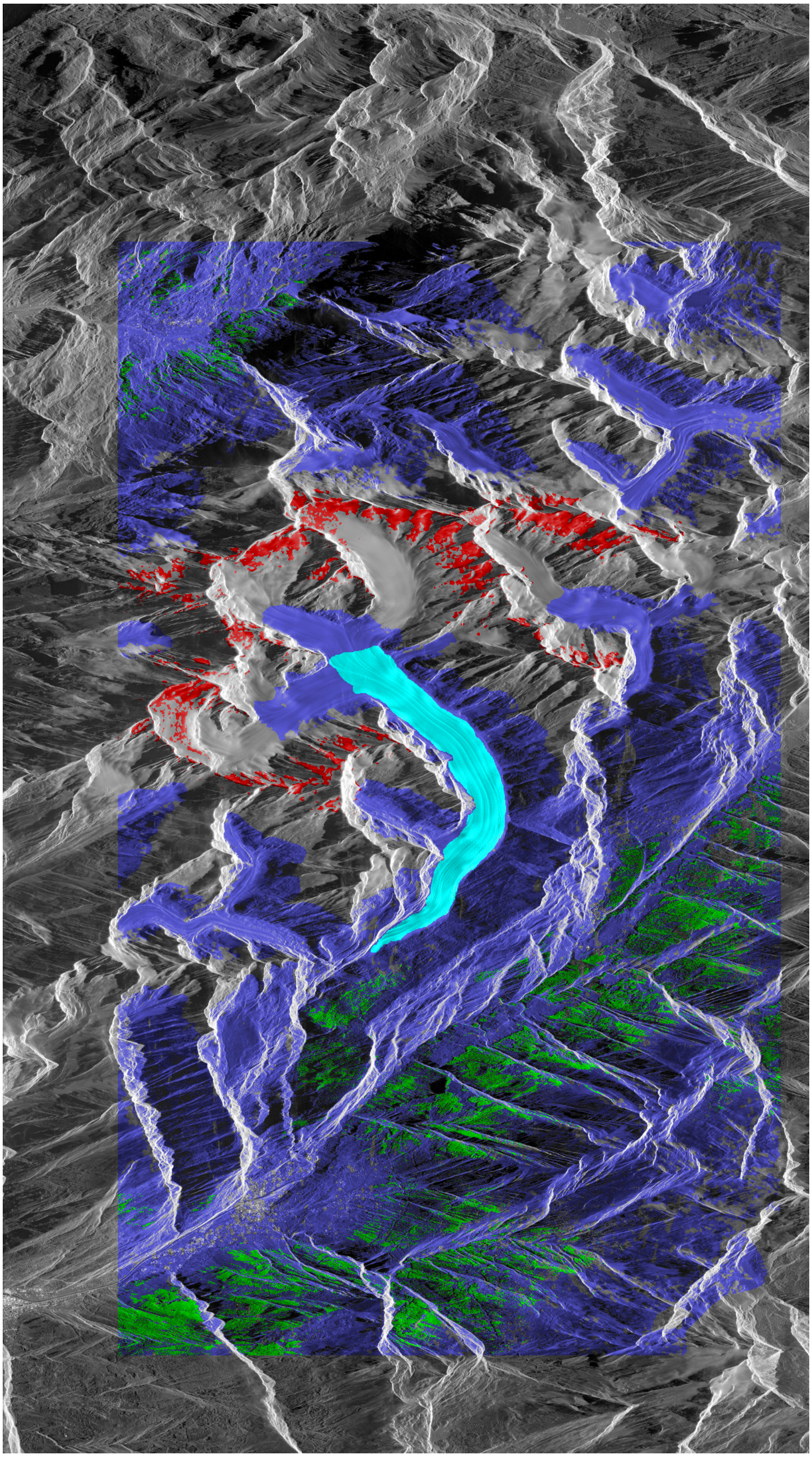

Figure S8. Mask used for the VV polarization indicating the three ROIs, the high accumulation area > 3500 m (red), the ablation area of Great Aletsch Glacier (cyan), and conifer forest (green), together with the mask used for calibration (blue). The masks in HH are very similar.

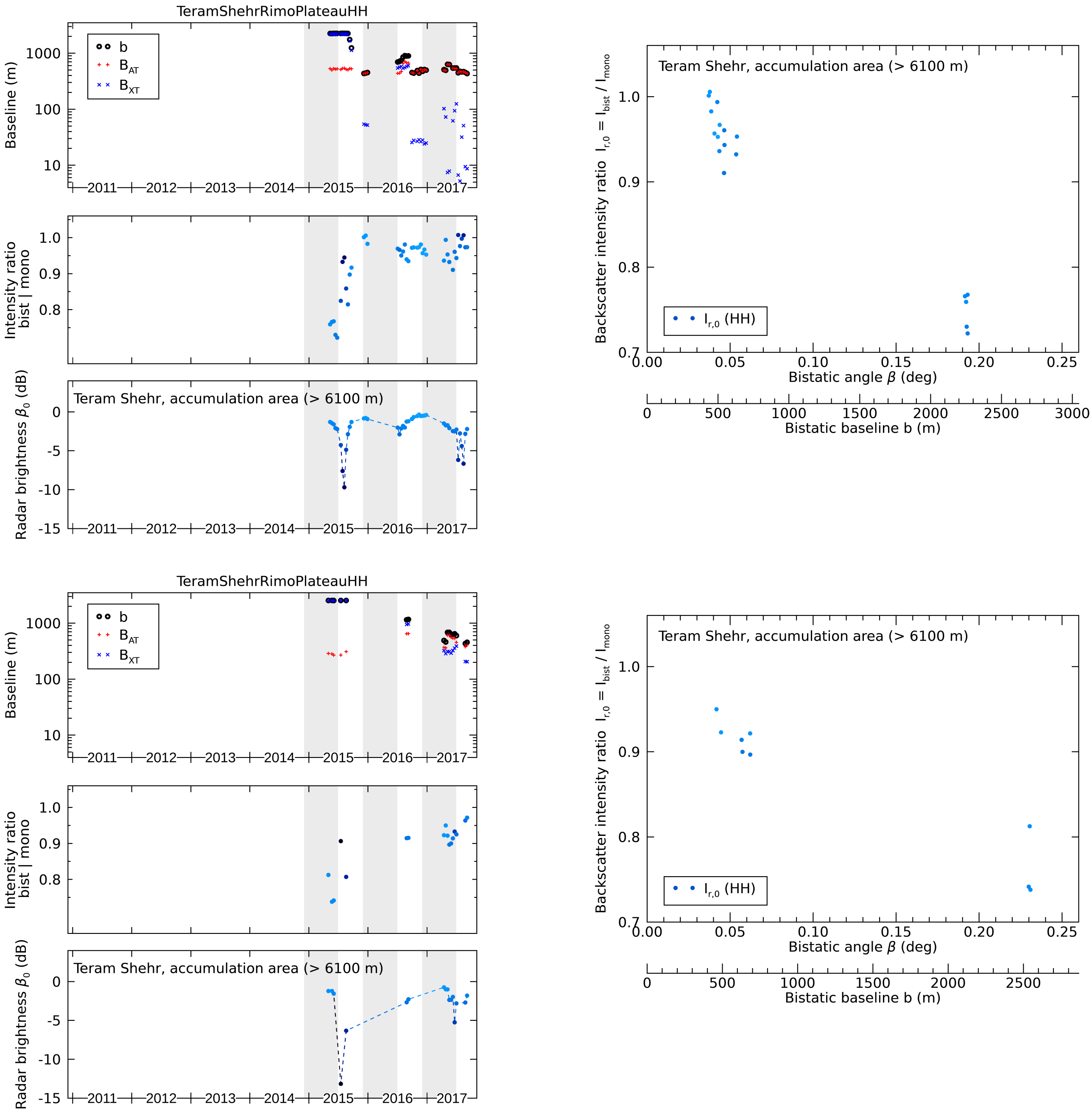

Figure S9. Time series of baselines b, B_{XT}, B_{AT}, bistatic-to-monostatic backscatter ratios $I_{r,0}$, and radar brightness $I_{mono} \equiv \beta_0$ for the accumulation area of Teram-Shehr glacier in the Karakorum. The right hand side shows $I_{r,0}$ over the bistatic angle β (1. December - 30. June).

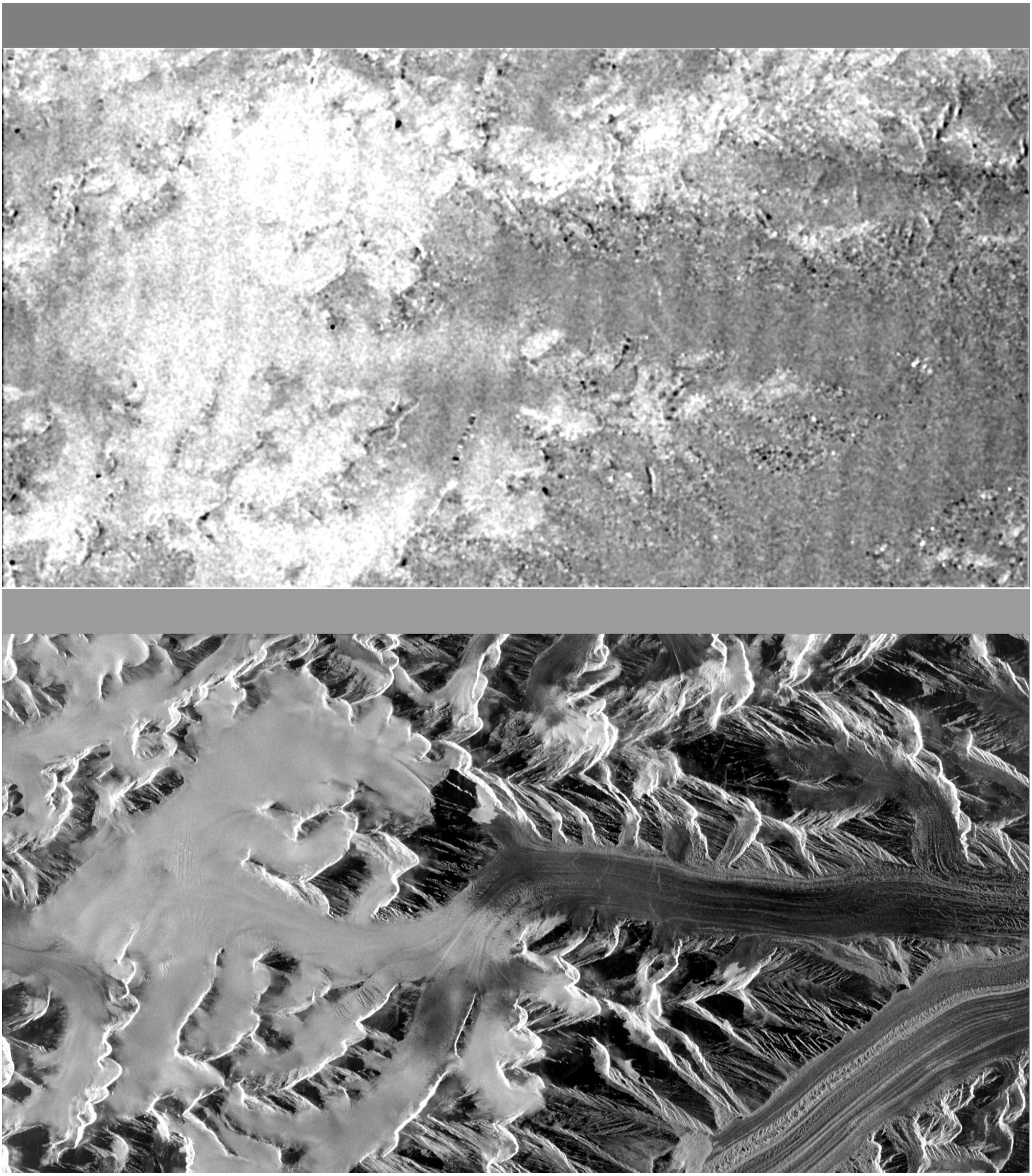

Figure S10. Top: monostatic-to-bistatic backscatter ratio $\hat{I}_{r,0}^{-1}$, observed by TanDEM-X on 2015-06-24 (orbit 075, descending) with $\beta = 0.19°$. Colorscale: [-1.5...+1.5 dB]. Bottom: Radar backscatter intensity for the same date. Colorscale: [-20..+5 dB]. Bright backscatter indicates dry snow in the accumulation area and dark snow indicates wet snow on the glacier tongue. Images shown in radar coordinates.

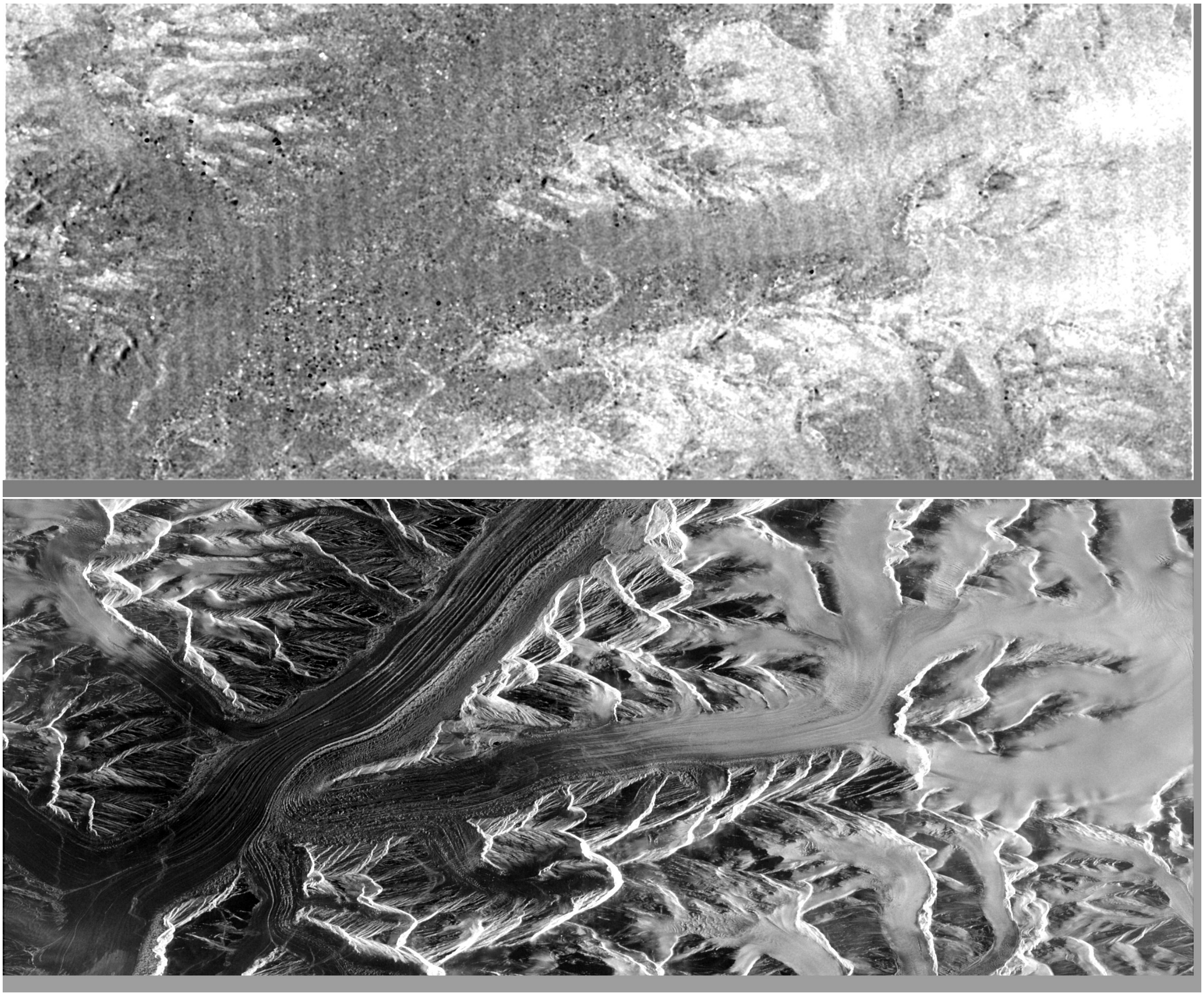

Figure S11. Top: monostatic-to-bistatic backscatter ratio $\hat{I}_{r,0}^{-1}$, observed by TanDEM-X on 2015-05-23 (orbit 098, ascending) with $\beta = 0.23°$. Colorscale: [-1.5...+1.5 dB]. Bottom: Radar backscatter intensity for the same date. Colorscale: [-20..+5 dB]. Bright backscatter indicates dry snow in the accumulation area and dark snow indicates wet snow on the glacier tongue. Images shown in radar coordinates.